PAPER

Check for updates

Quantifying the reaction mechanisms of a high-capacity CuP₂/C composite anode for potassium ion batteries†

Chen Zhao,[abc] Huixin Chen, [ID][bc] Haodong Liu,[d] Liang Yin,[f] Qiaobao Zhang, [ID][g] Sicen Yu,[d] Ping Liu, [ID][d] Guiming Zhong, [ID] *[abch] Can-Zhong Lu [ID] *[abch] and Yong Yang [ID][e]

Introducing metals into phosphorus to form metal phosphide materials as anodes for potassium ion batteries (PIBs) is an effective strategy to improve the electronic conductivity and alleviate the volume change during cycling, although with a compromise of capacity. Herein, we explore a CuP₂/C composite as a novel anode for PIBs, which delivers a high reversible capacity of >450 mA h g⁻¹. Unexpectedly, our results reveal that the PO$_x$ components existing in the prepared composite are reversible, through a quantitative analysis via high-resolution solid-state ³¹P NMR and synchrotron X-ray diffraction tests. Their potassiation products K_3PO_4 and $K_4P_2O_7$ can react with K−P alloys and turn back to PO$_x$ during depotassiation, which probably accounts for the high capacity of the prepared material. The results also illustrate a crystallization−amorphization evolution process during cycling involving nanocrystalline α-K_4P_6, K_4P_3 and KP, and amorphous K_4P_6, KP and K_3P phases, among which, the amorphous phases are identified for the first time.

1. Introduction

Aiming to develop low-cost high-energy-density electrochemical energy storage systems for smart power grids, smart cities and booming 5G applications, potassium ion batteries (PIBs) as a cost-effective option have attracted plenty of interest. The abundance of potassium resources and the replacement of Cu current collectors with Al ones lower the battery cost. Besides, previous research indicates that the standard potential of K⁺/K in organic solvents is 0.1 V vs. Li⁺/Li, which is a critical factor that determines the high energy density of PIBs.[1] K⁺ also shows a smaller Stokes radius in organic solvents such as propylene carbonate (PC) in spite of the larger ionic radius compared with Li⁺ and Na⁺, resulting in its higher ionic conductivity and transference number, which contribute to high-power PIBs.[2]

Hitherto, considerable efforts have been made to develop anode materials to improve the performance of batteries,[3–11] among which, phosphorus has drawn much attention due to

the possible formation of K_3P and can thus deliver the highest theoretical potassium storage capacity of 2596 mA h g⁻¹. Nevertheless, low intrinsic conductivity and large volume variation during cycling hinder its application. A clear understanding of the final products of P-based anode materials (P/C and MP$_x$/C) is still lacking. Some researchers proposed, on the basis of XRD and TEM measurements, that KP is the final product for phosphorus/carbon and FeP,[12,13] while some concluded, from XRD patterns, that K_4P_3 is generated for red P (rP)/N-doped carbon and GeP₅.[14,15] Furthermore, Jin et al. demonstrated the formation of K_3P by synchrotron XRD for a black phosphorus–graphite composite,[16] and Zhang et al. also showed the generation of K_3P for Sn_4P_3 material via XRD.[17,18] These studies have demonstrated the complexity of the investigation of P-based potassium storage anode materials. The final potassiation products may be diverse for different structures of P-based materials. What's more, despite many studies focusing on the exploration of P-based anode materials for PIBs

[a]College of Chemistry, Fuzhou University, Fuzhou 350108, Fujian, China

[b]CAS Key Laboratory of Design and Assembly of Functional Nanostructures, Fujian Provincial Key Laboratory of Nanomaterials, Fujian Institute of Research on the Structure of Matter, Chinese Academy of Sciences, Fuzhou 350002, Fujian, China. E-mail: gmzhong@fjirsm.ac.cn; czlu@fjirsm.ac.cn

[c]Xiamen Key Laboratory of Rare Earth Photoelectric Functional Materials, Xiamen Institute of Rare Earth Materials, Haixi institutes, Chinese Academy of Sciences, Xiamen 361021, Fujian, China

[d]Department of Nanoengineering, University of California San Diego, La Jolla, CA 92093, USA

[e]State Key Lab of Physical Chemistry of Solid Surfaces, Collaborative Innovation Center of Chemistry for Energy Materials and Department of Chemistry, Xiamen University, Xiamen 361005, Fujian, China

[f]X-ray Science Division, Advanced Photon Source, Argonne National Laboratory, Lemont, Illinois 60439, USA

[g]Department of Materials Science and Engineering, College of Materials, Xiamen University, Xiamen 361005, Fujian, China

[h]University of Chinese Academy of Sciences, Beijing, 100049, China

† Electronic supplementary information (ESI) available. See DOI: 10.1039/d0ta12141j

so far, the underlying reaction mechanisms of electrochemical (de)potassiation pathways and the final potassiation products of P-based materials have not been specifically understood, restricting further optimization. The possible formation of amorphous or nanocrystalline products of P-based anode materials and the indistinguishable strongest diffraction peaks for various crystalline K–P alloys make it quite challenging to precisely determine the products during cycling. Thus, exploring innovative P-based anode materials and employing appropriate characterization methods to understand the crucial factors affecting the (de)potassiation processes are very important for designing better-performance anodes for PIBs.

In this work, we explore a CuP_2/C composite as an anode material for PIBs, and present a systematic investigation into the potassium storage mechanisms of the material. We employ high-resolution solid-state ^{31}P NMR accompanied by high-energy synchrotron XRD measurements to gain quantitative insight into the amorphization–crystallization (de)potassiation reaction processes of the composite. The results unexpectedly reveal the reversibility of PO_x components in the composite,

which can deliver 2–3 potassium species per phosphorus. Besides, we observe that the contents of produced KP and K_3P during cycling are another critical factor influencing the capacity performance, while the undepotassiated K_4P_6 phase after cycling seriously affects the initial coulombic efficiency.

2. Results and discussion

2.1 Structures and morphologies of materials

Both CuP_2 and CuP_2/C materials were prepared by high-energy ball-milling, and their crystalline phases were verified by the XRD patterns (Fig. 1a), which obviously show that all the detected diffraction peaks are attributed to the CuP_2 phase (JCPDS No. 076-1190, monoclinic, S.G. $= P2_1/c$), indicating the successful synthesis of the target products without any crystalline residues or other binary compounds. Fig. S1a† shows the Raman spectra of the as-prepared CuP_2 and CuP_2/C materials, which clearly present several signals in the range of 200–500 cm^{-1} that are attributed to the CuP_2 phase which become weaker after ball-milling with carbon, which is probably due to
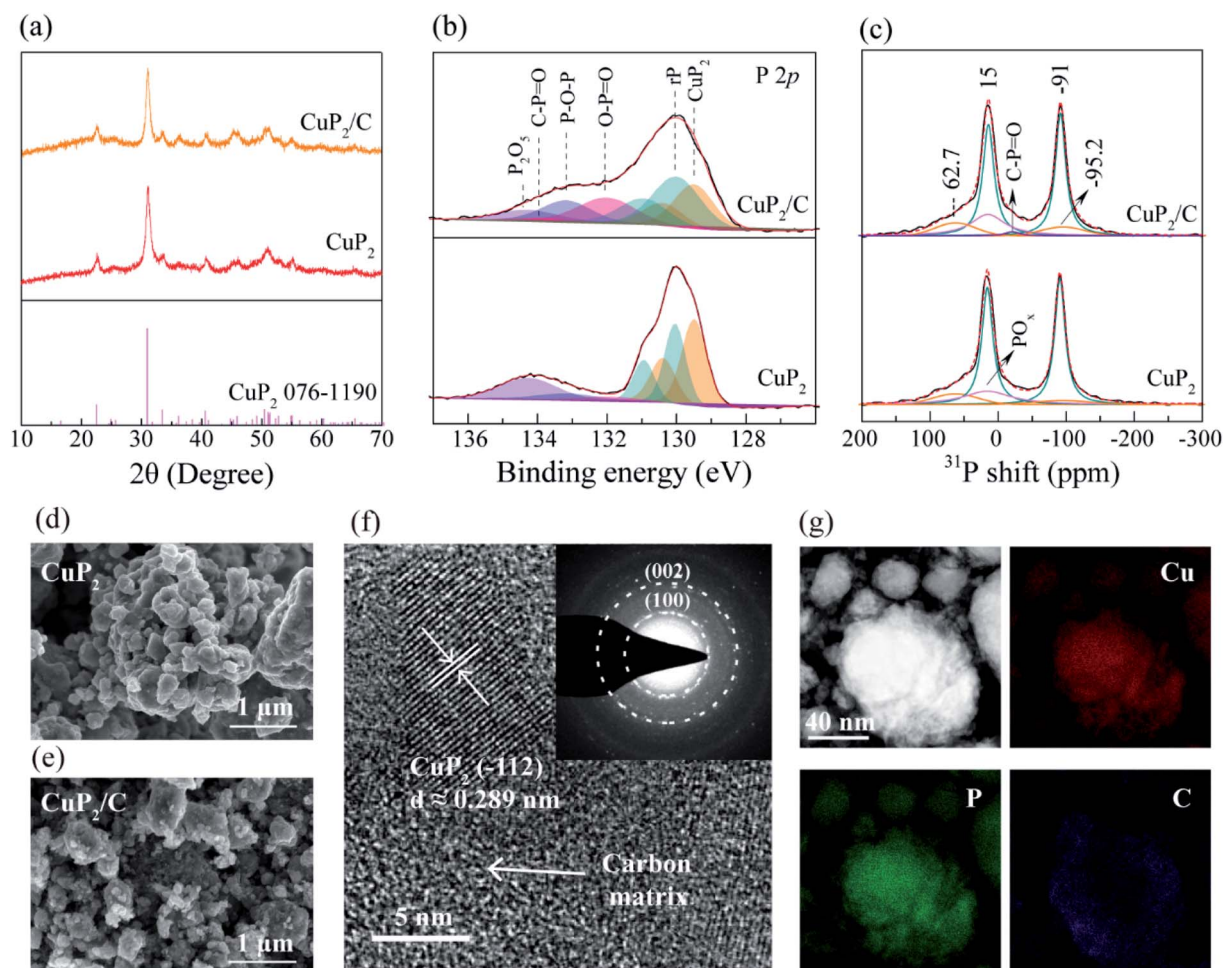
Fig. 1 The structural characterization of the as-synthesized CuP_2 and CuP_2/C materials: (a) XRD patterns, (b) XPS P 2p spectra, and (c) solid-state ^{31}P NMR spectra. The morphological characterization of the materials: SEM images of (d) CuP_2 and (e) CuP_2/C; (f) HR-TEM image of the CuP_2/C composite; the inset is the corresponding selected area electron diffraction (SAED) image; (g) elemental mapping images of the CuP_2/C composite.

the carbon coating on CuP_2. XPS spectra were recorded to better understand the components of the prepared materials. Fig. S1b† shows the Cu 2p spectra of CuP_2 and CuP_2/C, which display two characteristic peaks of Cu(I) 2p 3/2 and 1/2 at 932.9 and 952.6 eV.[19] In Fig. 1b, there is a broad P 2p peak at ~130 eV for both samples, corresponding to CuP_2 and unreacted rP. Besides, one broad peak at 134.3 eV related to P_2O_5 for the CuP_2 material is observed, where O element perhaps originates from the partially oxidized copper, phosphorus powder or impure inert atmosphere. After ball-milling, the broad peak clearly shifts to a lower binding energy, which is attributed to the formation of O–P=O (132.0 eV) and P–O–P (133.1 eV) bonds,[20] and the greatly reduced content of P_2O_5. The presence of O element is also evidenced by elemental analysis (Table S1†). Solid-state ^{31}P NMR spectra were further collected to gain a quantitative understanding on the prepared materials and are shown in Fig. 1c. Two intense ^{31}P NMR peaks located at 15 and −91 ppm (light cyan color) are observed for both samples, corresponding to two P sites in CuP_2 (Fig. S2†). Two other broad resonances at ~62.7 and ~−95.2 ppm (orange color) that are due to the unreacted rP are clearly shown in the fitting plots.[21] And a broad peak located at ~15 ppm (light magenta color) is distinguished and attributed to the P–O bonding. The very weak peak at ~−20 ppm (violet color) detected in CuP_2/C is assigned to the C–P=O bond, which is produced during the ball-milling process.[22] It is noted that the fitting analysis indicates that the atomic ratio of P in CuP_2, rP and P–O bonds (PO_x) is 7 : 1 : 2. In combination with the elemental analysis results (Table S1†) that show that the content of oxygen and carbon is 26.8% and 7.4%, respectively, we have calculated that the x value in PO_x is ~3.4, and conclude that the contents of CuP_2, rP, $PO_{3.4}$ and C in the composite are 50.2%, 3.5%, 19.5% and 26.8%, respectively. The results demonstrate that the as-prepared composite contains partial rP and P–O bonding (named PO_x), which mainly includes P–O–P and O–P=O bonds, and the P_2O_5 compound, as evidence by XPS results. It is mainly composed of the CuP_2 phase. For convenience, we still name the composite material CuP_2/C.

The CuP_2 material presents nanoparticles with irregular shape in the 300–600 nm size range agglomerating to secondary particles (Fig. 1d), while CuP_2/C shows many smaller particles in the 100–300 nm size range (Fig. 1e). The particle size distribution results are shown in Table S2.† D_{50} (median diameter) of CuP_2 is 647 nm, while that of CuP_2/C decreases to 303 nm, in good accord with the SEM results. The high-resolution TEM (HR-TEM) images and the elemental mapping results shown in Fig. 1f and g indicate that the CuP_2/C composite possesses a core–shell structure with the crystalline CuP_2 surrounded by carbon, which enhances the electronic conductivity of the composite.

2.2 Electrochemical results

Fig. 2a shows the cyclic voltammetry (CV) curves of the CuP_2/C composite for PIBs at a scan rate of 0.03 mV s^{-1}. During the initial cathodic sweep, a broad reduction peak appears in the range of 1.1–0.5 V, which is possibly due to the irreversible decomposition of electrolyte and the formation of a solid

electrolyte interface (SEI) on the fresh electrode surface. Afterwards, the current density continuously increases, indicating that the electrochemical potassiation process of the CuP_2/C electrode occurs. Thus, the first potassiation process of the CuP_2/C electrode may involve two steps. In the initial anodic sweep, a broad peak from 0 to 1.0 V and a pronounced peak centered at 1.1 V are observed, which demonstrate that the depotassiation process involves a two-step reaction. Notably, an apparent peak at 0.2 V is observed in the second discharge process, which implies a different reaction pathway compared to that in the first discharge. Fig. 2b shows the (dis)charge profiles of the CuP_2/C material for PIBs at a current density of 12.5 mA g^{-1}. The specific capacity reaches 806.4 mA h g^{-1} in the first discharge. A specific capacity of 476.7 mA h g^{-1} is recovered during charging, which is much higher than that reported for metal phosphides (MP_x, e.g. FeP and CoP) and is even comparable to that of some reported P/C materials.[23–25] The dQ/dV plot is shown in Fig. 2c, revealing very clear cathodic and anodic peaks that are almost in line with the CV results. This is due to the fact that the corresponding (dis)charge rate of the CV test is 1/27.8C, which is only ~1/2 of that using a current density of 12.5 mA g^{-1} for dQ/dV. What's more, the material presents a relatively stable cycling performance (Fig. 2d), which may be due to the introduction of Cu that alleviates the volume change during cycling. It is noticed that the material delivers a high initial discharge capacity of 806.4 mA h g^{-1} and a rechargeable capacity of 476.7 mA h g^{-1} (based on the mass of the composite, the same below). The value is higher than the theoretical values of 379.7 and 461.2 mA h g^{-1} of CuP_2/C (Tables S3 and S4†), which are calculated based on the formation of KP or K_4P_3, and include the capacity contributions of CuP_2, rP, reduced graphene oxide and Super P from the CuP_2/C composite, and the carbon nanotubes added during the electrode preparation process (a theoretical capacity of 279 mA h g^{-1} for carbon materials is employed for calculation).[15,26,27] The result indicates that the final potassiation products or the potassium storage mechanisms of the prepared CuP_2/C material may be different from those in previously reported studies. Unveiling the underlying potassium storage mechanism of the material that accounts for the high capacity may help to further design the high-performance P-based potassiation storage material. Here, we employed high-resolution solid-state ^{31}P NMR and high-energy synchrotron XRD techniques, expecting to carefully elucidate the final potassiation products and the phase change process of the composite during cycling.

2.3 Crystalline phase transformation by synchrotron XRD

Fig. 3 shows the high-energy ($\lambda_2 = 0.457926$ Å) synchrotron XRD patterns for the selected states, from which the crystalline products of the CuP_2/C material can be determined despite being beyond the detection limit of laboratory XRD ($\lambda_1 = 1.540598$ Å) (Fig. S3†). For the 1D0V state (discharge to 0 V in the first cycle, similarly hereinafter), the detected diffraction peaks at 7.6, 8.2 and 8.4° (‡) can be well indexed to the KP phase (JCPDS No. 071-1844) according to the standard PDF cards of K–P alloys. The signals at 7.8, 10.2 and 12.5° (§) are ascribed to
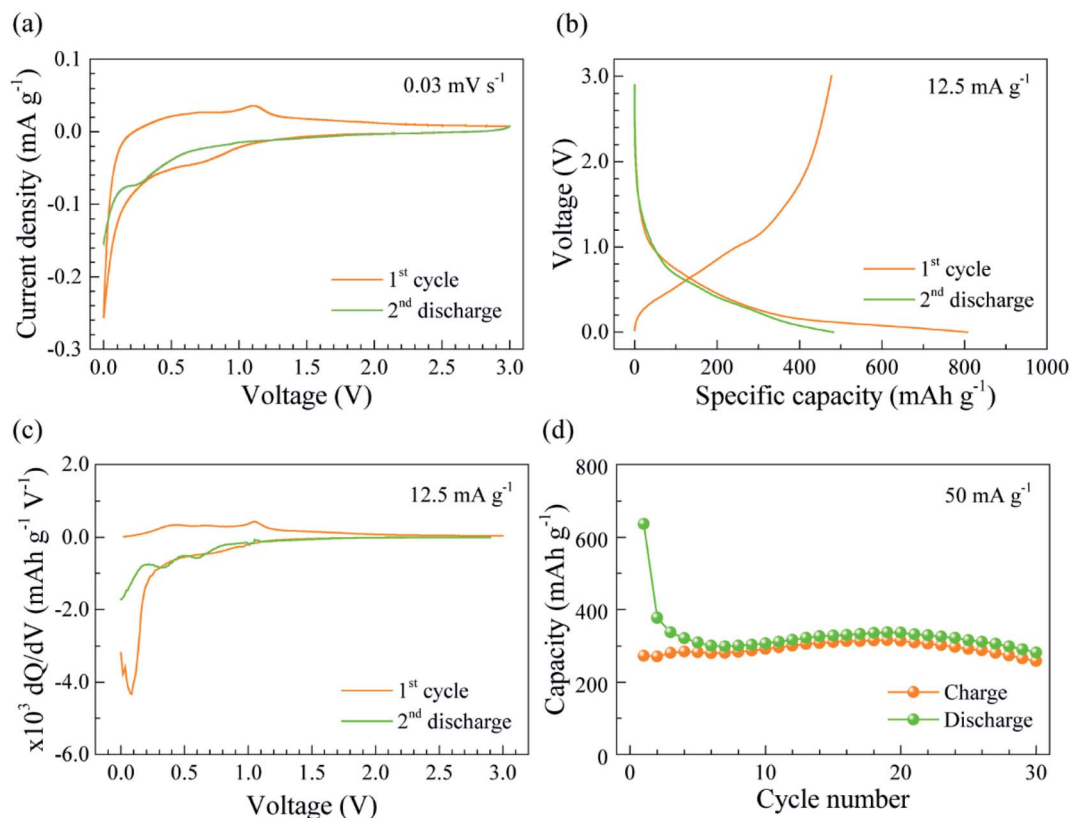
Fig. 2 The electrochemical tests of the CuP_2/C material as an anode for PIBs: (a) CV curves at a scan rate of 0.03 mV s^{-1} and (b) electrochemical profiles in the first cycle and second discharge process at 12.5 mA g^{-1}. (c) Differential capacity plots of the first cycle and second discharge at 12.5 mA g^{-1}. (d) Cycling performance at 50 mA g^{-1}. The specific capacity and applied current densities are based on the mass of the CuP_2/C composite.

the K_4P_3 phase (JCPDS No. 079-0033). Besides, we observe the diffraction peaks of $K_4P_2O_7$ at 7.7, 8.9, 12.1 and 12.7° (*) for the state, which is probably the potassiation product of PO_x. It is noticeable that the detected peaks at 4.8, 7.2 and 8.6° for the 1D0V state are assigned to potassium fluorophosphates such as KPO_2F_2, K_2PO_3F and $K_2P_2O_5F_2$ (Fig. S4†), which may be due to the decomposition of KPF_6 during the *ex situ* test. Other diffraction peaks at ~9, 9.5 and 11° are difficult to distinguish due to the close diffraction signals for these K–P alloys. Unexpectedly, these diffraction peaks including signals of $K_4P_2O_7$ almost completely vanish at the 1C3.0V (charge to 3.0 V in the first cycle, similarly hereinafter) state, which indicates that amorphous products are possibly generated and $K_4P_2O_7$ may react to form other compounds. Moreover, a new diffraction peak at 6.7° (†) is detected for the 1C3.0V state, which can be assigned to P_2O_5, indicating that $K_4P_2O_7$ may transform to PO_x during charging. At the second discharged state (2D0V, discharge to 0 V in the second cycle, similarly hereinafter), the diffraction signals of K_4P_3, KP and $K_4P_2O_7$ phases emerge again. These results reveal that KP and K_4P_3 are possibly the main final electrochemical potassiation products of the CuP_2 material. What's more, our results demonstrate that PO_x is probably an active material for potassium storage, which can recover after cycling. Besides, all the detected diffraction peaks show low

intensities, which indicates that the reaction products are probably nano-crystalline or amorphous.

2.4 Solid-state ^{31}P NMR spectroscopy

Solid-state ^{31}P NMR spectroscopy was further employed here to determine both the amorphous and crystalline P-containing products during the (de)potassiation. Fig. S5† presents the solid-state ^{31}P NMR spectra of the prepared standard K–P alloys, the details of which will be discussed in a separate study. The results show that the ^{31}P NMR resonances of crystalline α-K_4P_6 and β-K_4P_6 are −114 and −81 ppm, respectively. And the resonances of crystalline KP, K_4P_3 and K_3P phases are ~−220, 150 and 425 ppm, respectively. It is worth mentioning that the resonance of the compound may shift due to the non-stoichiometric or the amorphous state.[28,29] The fitting details of the spectra of CuP_2/C electrodes at different states are illustrated in the ESI.† Briefly, the peaks at ~11.6 and ~0 ppm are attributed to K_3PO_4 and $K_4P_2O_7$.[30,31] Four peaks from −180 to −275 ppm can be deconvoluted, including two sharp peaks at ~−255 and −272 ppm, and two broad peaks at ~−180 and −225 ppm, which are probably due to the nonstoichiometric and amorphous KP phases, respectively. The very broad peak at −55 ppm is possibly due to the a-K_4P_6 (amorphous β-K_4P_6, similarly hereinafter). Beyond that, the peaks at ~210 and 450 ppm are ascribed to K_4P_3 and K_3P, respectively.
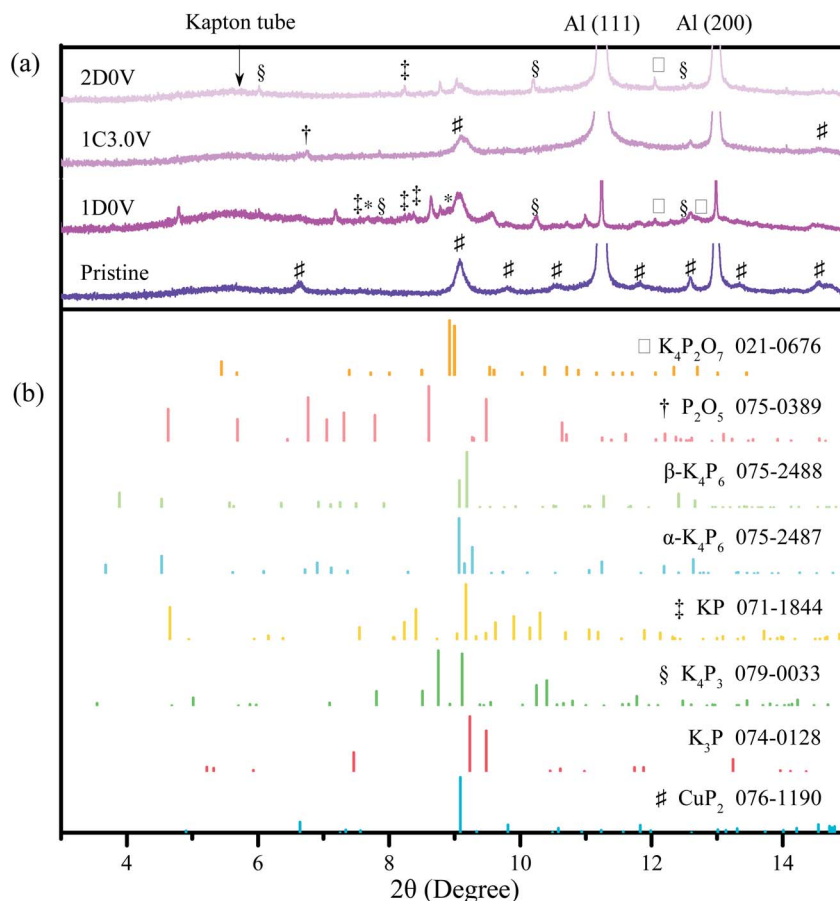
Fig. 3 (a) Synchrotron XRD patterns of CuP_2/C electrodes at selected states; (b) standard PDF cards of $K_4P_2O_7$, P_2O_5, α-K_4P_6, β-K_4P_6, KP, K_4P_3, K_3P and CuP_2.

Fig. 4 shows the mass-normalized ^{31}P NMR spectra of CuP_2/C electrodes during the first cycle. As the voltage falls to 0.5 V (1D0.5V), two peaks at 11.6 and $\sim$0 ppm emerge accompanied by the disappearance of a broad peak at around 10 ppm in comparison to the pristine state, indicating that PO_x is potassiated to produce K_3PO_4 and $K_4P_2O_7$ during this process. Additionally, two broad weak peaks at ~-55 and ~-185 ppm attributed to a-K_4P_6 and KP phases are also observed. The ^{31}P NMR spectrum of 1D0.33V shows a similar profile to that of 1D0.5V except for a slight increase in the intensity of the signals at -55 and -180 ppm. Therefore, we can conclude that the discharge process from the pristine to the 1D0.33V state is mainly the potassiation reaction of PO_x to produce K_3PO_4 and $K_4P_2O_7$, along with a potassiation reaction of a small amount of CuP_2 and rP to form a-K_4P_6 and KP. As the CuP_2 is discharged to lower than 0.33 V, the signals at ~-55 ppm and -180 to -275 ppm increase continuously with discharging, accompanied by the reducing intensities of the signals of CuP_2 and rP, which corresponds to the formation of a-K_4P_6 and KP phases. A broad weak peak at ~450 ppm emerges as the discharge voltage reaches 0.05 V (1D0.05V), and its intensity increases as the voltage becomes 0 V, demonstrating the formation of K_3P. At the same time, the broad peak at ~220 ppm is detected for 1D0V, which is ascribed to the formation of K_4P_3. Thus, we can

conclude that a-K_4P_6 and KP are mainly produced from 0.33 V to 0.05 V in the first discharge, while KP, K_4P_3 and K_3P are the main products from 0.05 V to 0 V.

During charging, the intensity of a-K_4P_6 at -55 ppm decreases and the signals of K_4P_3 at ~220 ppm and K_3P at ~450 ppm vanish, while the peak of crystalline α-K_4P_6 at -115 ppm emerges as the voltage rises to 0.78 V (1C0.78V). Meanwhile, the sharp peaks attributed to crystalline KP at ~-255 and -272 ppm increase until the voltage reaches 0.78 V. These results reveal that a complex transformation process of amorphous phases to crystalline phases occurs during the depotassiation process from 1D0V to 1C0.78V. From 1C0.78V to 1C0.96V, the intensity of crystalline α-K_4P_6 keeps increasing. A weak signal at ~46 ppm with an integral area ratio of less than 4% and a half-width of ~9 ppm can be detected from 1C0.54V to 1C0.96V, and it vanishes as the cell is charged to 1.2 V, which may be due to the formation of the nonstoichiometric K–P phase. The signal is also detected at the 2D0.24V state, and we find that the corresponding phase mainly exists with the crystalline α-K_4P_6 (-116 ppm). Therefore, we conclude that the signal of ~46 ppm is possibly due to the nonstoichiometric $K_{4+x}P_6$ phase. Note that the crystalline α-K_4P_6 signal at -116 ppm and KP signals at -180 to -275 ppm reduce apparently for 1C1.2V compared to 1C0.96V, while a significant
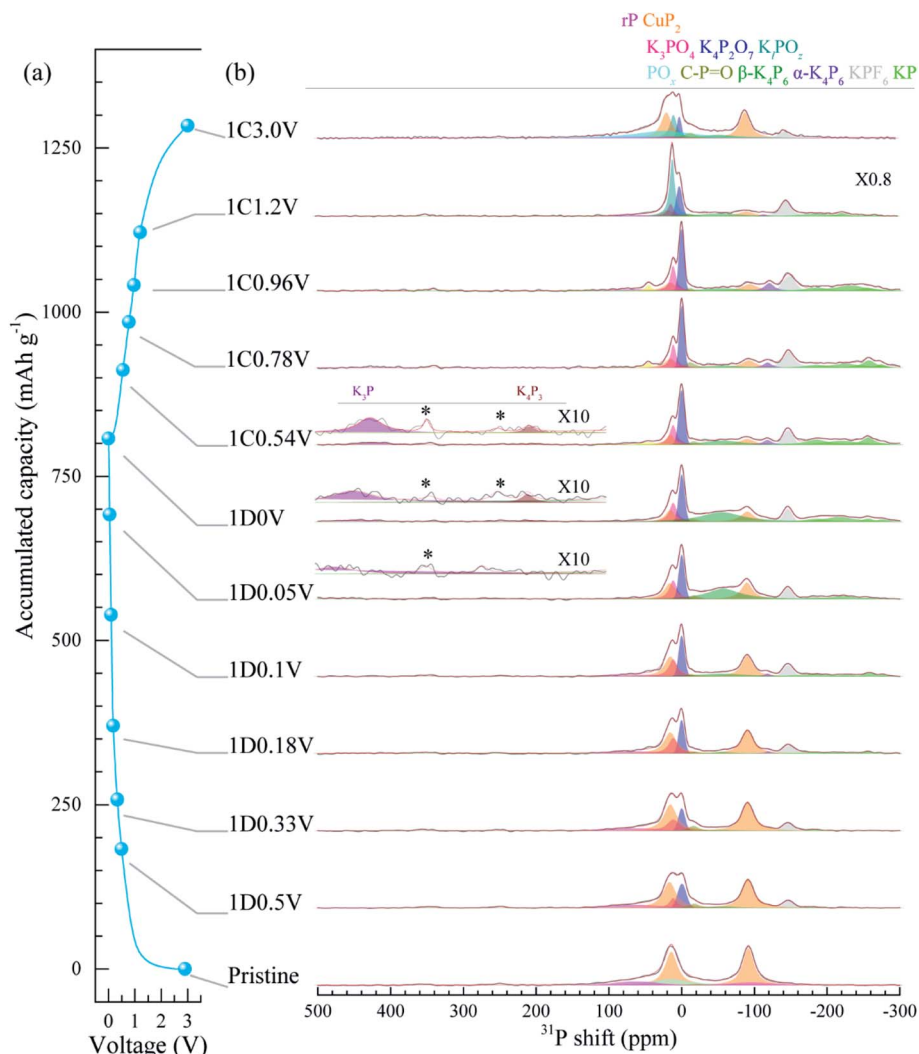
Fig. 4 Tracking the structural evolution of the CuP$_2$/C composite in the first cycle by solid-state ^{31}P NMR spectroscopy: (a) the electrochemical profiles of the CuP$_2$/C electrode cycling at a current density of 12.5 mA g^{-1}; (b) solid-state ^{31}P NMR spectra of the CuP$_2$/C electrodes at selected states (light grey colored peak at ∼−145 ppm: the residual KPF$_6$ originating from the electrolytes; purple colored area: K$_3$P; wine colored area: K$_4$P$_3$; magenta colored area: rP; orange colored area: CuP$_2$; pink colored area: K$_3$PO$_4$; navy colored area: K$_4$P$_2$O$_7$; dark cyan colored area: K$_l$PO$_z$; dark yellow colored area: C−P═O; cyan colored area: PO$_x$; olive colored area: a-K$_4$P$_6$; violet colored area: α-K$_4$P$_6$; green colored area: KP; the asterisks indicate the spinning sidebands).

change for the signals at around 0 ppm is observed. In order to give a converged fitting result, another intense signal at ∼8 ppm with a half-width of ∼8 ppm needs to be added in addition to the signals at 0, 11.6 and 15.6 ppm from K$_4$P$_2$O$_7$, K$_3$PO$_4$ and CuP$_2$, respectively (Fig. S6† shows a comparison of fitting results by using 3 peaks and 4 peaks at ∼0 ppm). As the voltage rises to 3.0 V, the sharp signal at ∼8 ppm greatly reduces, while the peak at ∼−92 ppm attributed to CuP$_2$ increases and a broad signal ranging from 70 to −150 ppm emerges. According to the quantitative fitting results of the spectra shown in Table S5,† we find that the signal at ∼8 ppm emerges with the content decrease of K$_4$P$_2$O$_7$, KP and α-K$_4$P$_6$ phases. The signal reduces from 26.3% for 1C0.96V to 10.9% for 1C1.2V with the increase of CuP$_2$ by 15.6%, rP by 2.2% and PO$_x$ by 30.7%, and the reduction of K–O–P by 17.1% from 1C1.2V to 1C3.0V. Besides, the ^{31}P resonance at 8 ppm does not match any K–P alloy references

(Fig. S5†). Therefore, we consider that the peak at ∼8 ppm may be due to an intermediate phase between PO$_x$ and K$_4$P$_2$O$_7$ or K$_3$PO$_4$. Here we labelled it K$_l$PO$_z$. Surprisingly, the corresponding fitting result of 1C3.0V shows that the signal at 11.6 ppm corresponding to K$_3$PO$_4$ almost vanishes and the peak at 0 ppm attributed to K$_4$P$_2$O$_7$ also dramatically reduces, while the signals at −92 and 15.6 ppm from CuP$_2$ and 62.7 and −95.2 ppm from rP increase. And a broad signal at ∼10 ppm ascribed to PO$_x$ is detected again at 1C3.0V, which is highly required to meet a convergent fitting. These results are highly consistent with the XRD data, which reveal that PO$_x$ recovers after charging, presenting its reversibility as an anode for PIBs. This is analogous to the SiO$_x$ anode material for lithium ion batteries, for which it has been shown that the produced Li$_4$SiO$_4$ during lithiation will react with the Li$_x$Si alloy to form SiO$_x$ and Si during the delithiation process.[32]

We also recorded the ^{31}P NMR spectra for the second discharge process, as shown in Fig. S7.† As the material is discharged to 0.78 V (2D0.78V), the intensity of CuP$_2$ almost remains the same, while the profile at around 0 ppm significantly changes. The fitting results of 2D0.78V and 2D0.42V show that the broad peak at ~10 ppm vanishes and the peaks at ~0 and ~11.6 ppm keep increasing until the voltage reduces to 0.42 V, demonstrating that the potassiation reaction of PO$_x$ to K$_3$PO$_4$ and K$_4$P$_2$O$_7$ occurs during the process. From 2D0.78V to 2D0.42V, we also find that the peaks at 15.6 and ~−92 ppm greatly reduce, accompanied by an increase in the intensity of the signal at ~−116 ppm and a broad signal at ~−220 ppm, indicating the reaction of CuP$_2$ to form crystalline α-K$_4$P$_6$ and KP phases in the process. Afterwards, the signal of crystalline α-K$_4$P$_6$ at −116 ppm decays, and the KP signals at around −230 and −255 ppm increase for 2D0.24V compared to 2D0.42V, which hints at the potassiation of crystalline α-K$_4$P$_6$ to form KP. As the voltage decreases to 0 V in the second discharge, the signals of K$_4$P$_3$ at ~220 and K$_3$P at 450 ppm appear. The spectra also show that the intensity of the broad peak at −55 ppm from a-K$_4$P$_6$ keeps increasing as the voltage is lower than 0.24 V. And the sharp peak at −255 ppm almost disappears at the 2D0V state, revealing that the KP product is inclined to be amorphous at a deep potassiation state. Therefore, we conclude that α-K$_4$P$_6$ is inclined to firstly form for the second cycle in comparison to the initial discharge process.

2.5 Discussion

To gain further insight into the complex phase transformation of the CuP$_2$/C composite, quantitative analysis of the phase changes upon cycling based on the ^{31}P NMR spectra is presented in Fig. 5. The results clearly uncover the reversibility of different components including CuP$_2$, rP and PO$_x$, and reveal that PO$_x$ is rechargeable. The theoretical capacity of PO$_x$ (as x equals 3.4) can reach 755.1 mA h g^{-1} according to eqn (1), assuming that the final products are KP, K$_3$PO$_4$ and K$_4$P$_2$O$_7$, which is higher than that of CuP$_2$ (427 mA h g^{-1}, taking KP as the final product). The theoretical capacity contribution of PO$_{3.4}$ in the composite is 147.5 mA h g^{-1} (Table S4†). Both previous studies and our electrochemical results display that MP$_x$ including FeP, CoP and CuP$_2$ exhibit relatively good reversibility as anodes for PIBs.[33–35] However, the quantitative analysis from the solid-state ^{31}P NMR study exposes that only ~35% of CuP$_2$ in the composite recovers after charging. In contrast, a high reversibility of PO$_x$ is discovered. Note that the content of PO$_x$ in the cycled state is much higher than that in the pristine material, which is possibly due to the structural reconstruction that causes the change of atomic ratio of P and O elements. It's worth noting that although CuP$_2$ does not recover after charging, most of the produced K–P and K–O–P compounds depotassiate to generate PO$_x$, rP and CuP$_2$ during charging. And the total content of rechargeable P reaches 80%. This is the most probable reason for the reported high reversibility of MP$_x$
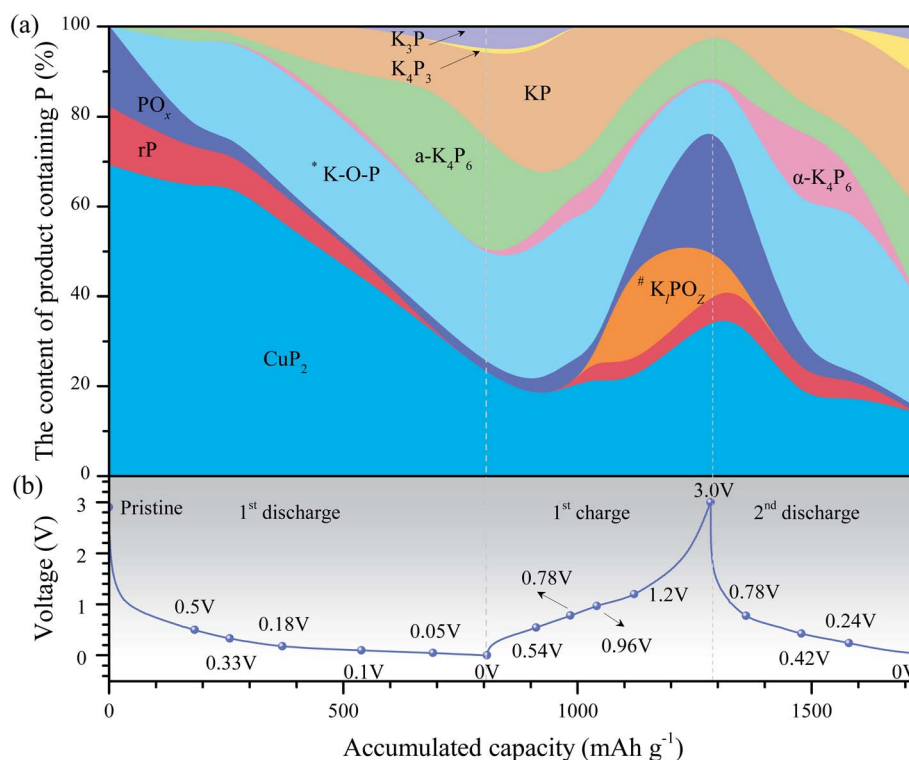
Fig. 5 (a) Phase transformation diagram for the CuP$_2$/C composite with the galvanostatic (dis)charge processes; the contents of produced K–P alloys and K–P–O compounds can be directly read in the Y axis, depending on the deconvolution results of *ex situ* ^{31}P NMR spectra in Fig. 4 and S7.† (b) The electrochemical cycling profiles of the CuP$_2$/C electrode at a current density of 12.5 mA g^{-1}. *K–P–O indicates K$_4$P$_2$O$_7$ and K$_3$PO$_4$. #K$_l$PO$_z$ indicates an intermediate phase between PO$_x$ and K$_4$P$_2$O$_7$ or K$_3$PO$_4$.

for PIBs.[36,37] The rechargeable P content of 80% based on the solid-state NMR results is much higher than the corresponding practical coulombic efficiency (CE) of 59%, which is due to the dramatic decomposition of the electrolyte that decreases the CE.[38] Beyond that, residual K–P alloys such as a-K_4P_6 and $K_4P_2O_7$ at the charged state are critical factors that cause the low initial coulombic efficiency. These findings offer a new pathway whereby the content and bonding properties of oxygen for the P-based anodes can be adjusted to improve the capacity with balanced volume change during cycling. We also find that decreasing the residual contents of K_4P_6 and $K_4P_2O_7$ products is very important for improving the initial coulombic efficiency and thus the reversible capacity performance. Through optimization of the morphology along with the additive, binder and electrolyte to enhance the ionic transport, we believe that the performance of such type of material, especially the cycling stability, should be further improved.

$$5.12PO_{3.4} + 12.32K \rightleftharpoons 2.6K_3PO_4 + K_4P_2O_7 + 0.52KP \quad (1)$$

Fig. 5 also reveals that KP and a-K_4P_6 are the main products of CuP_2 for PIBs. Small amounts of K_4P_3 and K_3P still form after discharge. In the second cycle, the contents of KP, K_4P_3 and K_3P increase, which may be caused by the decreasing particle sizes during cycling that would shorten the ionic transport path for reducing the polarization. For the crystalline states of the final potassiation products, the high-energy synchrotron XRD patterns only show very weak diffraction peaks of $K_4P_2O_7$, KP and K_4P_3 at 1D0V, whose intensities decrease obviously at 2D0V. This indicates that the final potassiation products of the material, such as KP, K_3PO_4 and K_3P, are mainly amorphous, and become more disordered after cycling. The deduction is even evidenced by the NMR spectra, which show that the sharp peaks at −255 and −272 ppm attributed to crystalline KP at 2D0V are almost undetected. Besides, the results still reveal that a complex crystallization–amorphization transformation process takes place for K–P alloys during cycling. a-K_4P_6 mainly forms in the first potassiation process, while crystalline α-K_4P_6 is generated during depotassiation, implying different reaction pathways for the (de)potassiation processes. During the second potassiation process, the crystalline α-K_4P_6 is firstly produced, the content of which reduces with further potassiation and then the formation of a-K_4P_6 dominates.

3.   Conclusions

In conclusion, our results suggest that PO_x components in the CuP_2/C composite exhibit good reversibility. They are potassiated to form K_3PO_4 and $K_4P_2O_7$, which would react with K–P alloys to regenerate the PO_x during the depotassiation process. This is a critical factor that accounts for the high reversible capacity of 476.7 mA h g^{-1} for the CuP_2/C composite. The results also confirm for the first time the formation of amorphous K_3P, KP and K_4P_6. Our work on PIBs depicts a quantitative understanding on the reaction

mechanisms of the CuP_2/C composite, which paves a new road to design high-capacity P-based potassium storage anode materials by adjusting the content and bonding properties of oxygen.

Conflicts of interest

There are no conflicts to declare.

Acknowledgements

References

1 K. Kubota, M. Dahbi, T. Hosaka, S. Kumakura and S. Komaba, Towards K-Ion and Na-Ion Batteries as "Beyond Li-Ion", *Chem. Rec.*, 2018, **18**(4), 459–479.

2 T. Hosaka, K. Kubota, A. S. Hameed and S. Komaba, Research Development on K-Ion Batteries, *Chem. Rev.*, 2020, **120**(14), 6358–6466.

3 Z. Liu, X.-Y. Yu, X. W. Lou and U. Paik, Sb@C coaxial nanotubes as a superior long-life and high-rate anode for sodium ion batteries, *Energy Environ. Sci.*, 2016, **9**(7), 2314–2318.

4 E. Edison, R. Satish, W. C. Ling, N. Bucher, V. Aravindan and S. Madhavi, Nanostructured intermetallic $FeSn_2$-carbonaceous composites as highly stable anode for Na-ion batteries, *J. Power Sources*, 2017, **343**, 296–302.

5 S. Qiu, L. Xiao, X. Ai, H. Yang and Y. Cao, Yolk–Shell TiO_2@C Nanocomposite as High-Performance Anode Material for Sodium-Ion Batteries, *ACS Appl. Mater. Interfaces*, 2017, **9**(1), 345–353.

6 J.-G. Wang, H. Sun, H. Liu, D. Jin, R. Zhou and B. Wei, Edge-oriented SnS_2 nanosheet arrays on carbon paper as advanced binder-free anodes for Li-ion and Na-ion batteries, *J. Mater. Chem. A*, 2017, **5**(44), 23115–23122.

7 C. Luo, G. L. Xu, X. Ji, S. Hou, L. Chen, F. Wang, J. Jiang, Z. Chen, Y. Ren, K. Amine and C. Wang, Reversible Redox Chemistry of Azo Compounds for Sodium-Ion Batteries, *Angew. Chem., Int. Ed. Engl.*, 2018, **57**(11), 2879–2883.

8 Y. Wu, Z. Liu, X. Zhong, X. Cheng, Z. Fan and Y. Yu, Amorphous Red Phosphorus Embedded in Sandwiched Porous Carbon Enabling Superior Sodium Storage Performances, *Small*, 2018, **14**(12), e1703472.

9   J. Fullenwarth, A. Darwiche, A. Soares, B. Donnadieu and L. Monconduit, NiP₃: a promising negative electrode for Li- and Na-ion batteries, *J. Mater. Chem. A*, 2014, **2**(7), 2050–2059.

10 Y. Cheng, Z. Yao, Q. Zhang, J. Chen, W. Ye, S. Zhou, H. Liu and M. S. Wang, In Situ Atomic-Scale Observation of Reversible Potassium Storage in Sb₂S₃@Carbon Nanowire Anodes, *Adv. Funct. Mater.*, 2020, **30**(52), 2005417.

11 Y. Li, Q. Zhang, Y. Yuan, H. Liu, C. Yang, Z. Lin and J. Lu, Surface Amorphization of Vanadium Dioxide (B) for K-Ion Battery, *Adv. Energy Mater.*, 2020, **10**(23), 2000717.

12 I. Sultana, M. M. Rahman, T. Ramireddy, Y. Chen and A. M. Glushenkov, High capacity potassium-ion battery anodes based on black phosphorus, *J. Mater. Chem. A*, 2017, **5**(45), 23506–23512.

13 P. Xiong, P. Bai, S. Tu, M. Cheng, J. Zhang, J. Sun and Y. Xu, Red Phosphorus Nanoparticle@3D Interconnected Carbon Nanosheet Framework Composite for Potassium-Ion Battery Anodes, *Small*, 2018, **14**(33), 1802140.

14 Y. Wu, S. Hu, R. Xu, J. Wang, Z. Peng, Q. Zhang and Y. Yu, Boosting Potassium-Ion Battery Performance by Encapsulating Red Phosphorus in Free-Standing Nitrogen-Doped Porous Hollow Carbon Nanofibers, *Nano Lett.*, 2019, **19**(2), 1351–1358.

15 W. Zhang, Z. Wu, J. Zhang, G. Liu, N.-H. Yang, R.-S. Liu, W. K. Pang, W. Li and Z. Guo, Unraveling the effect of salt chemistry on long-durability high-phosphorus-concentration anode for potassium ion batteries, *Nano Energy*, 2018, **53**, 967–974.

16 H. Jin, H. Wang, Z. Qi, D.-S. Bin, T. Zhang, Y. Wan, J. Chen, C. Chuang, Y.-R. Lu, T.-S. Chan, H. Ju, A.-M. Cao, W. Yan, X. Wu, H. Ji and L.-J. Wan, Black Phosphorus–Graphite Composite Anode for Li-/Na-/K-Ion Batteries, *Angew. Chem., Int. Ed.*, 2020, **59**(6), 2318–2322.

17 W. Zhang, W. K. Pang, V. Sencadas and Z. Guo, Understanding High-Energy-Density Sn₄P₃ Anodes for Potassium-Ion Batteries, *Joule*, 2018, **2**(8), 1534–1547.

18 W. Zhang, J. Mao, S. Li, Z. Chen and Z. Guo, Phosphorus-Based Alloy Materials for Advanced Potassium-Ion Battery Anode, *J. Am. Chem. Soc.*, 2017, **139**(9), 3316–3319.

19 A. Y. Kim, M. K. Kim, K. Cho, J.-Y. Woo, Y. Lee, S.-H. Han, D. Byun, W. Choi and J. K. Lee, One-Step Catalytic Synthesis of CuO/Cu₂O in a Graphitized Porous C Matrix Derived from the Cu-Based Metal–Organic Framework for Li- and Na-Ion Batteries, *ACS Appl. Mater. Interfaces*, 2016, **8**(30), 19514–19523.

20 P. Nakhanivej, X. Yu, S. K. Park, S. Kim, J.-Y. Hong, H. J. Kim, W. Lee, J. Y. Hwang, J. E. Yang, C. Wolverton, J. Kong, M. Chhowalla and H. S. Park, Revealing molecular-level surface redox sites of controllably oxidized black phosphorus nanosheets, *Nat. Mater.*, 2019, **18**(2), 156–162.

21 A. Bytchkov, F. Fayon, D. Massiot, L. Hennet and D. L. Price, ³¹P solid-state NMR studies of the short-range order in phosphorus-selenium glasses, *Phys. Chem. Chem. Phys.*, 2010, **12**(7), 1535–1542.

22 S.-O. Kim and A. Manthiram, The facile synthesis and enhanced sodium-storage performance of a chemically

bonded CuP₂/C hybrid anode, *Chem. Commun.*, 2016, **52**(23), 4337–4340.

23 W. Zhang, J. Mao, S. Li, Z. Chen and Z. Guo, Phosphorus-Based Alloy Materials for Advanced Potassium-Ion Battery Anode, *J. Am. Chem. Soc.*, 2017, **139**(9), 3316–3319.

24 X. Wu, W. Zhao, H. Wang, X. Qi, Z. Xing, Q. Zhuang and Z. Ju, Enhanced capacity of chemically bonded phosphorus/carbon composite as an anode material for potassium-ion batteries, *J. Power Sources*, 2018, **378**, 460–467.

25 Q. Liu, Z. Hu, Y. Liang, L. Li, C. Zou, H. Jin, S. Wang, H. Lu, Q. Gu, S.-L. Chou, Y. Liu and S.-X. Dou, Facile Synthesis of Hierarchical Hollow CoP@C Composites with Superior Performance for Sodium and Potassium Storage, *Angew. Chem.*, 2020, **132**(13), 5197–5202.

26 Y. Wang, Z. Wang, Y. Chen, H. Zhang, M. Yousaf, H. Wu, M. Zou, A. Cao and R. P. S. Han, Hyperporous Sponge Interconnected by Hierarchical Carbon Nanotubes as a High-Performance Potassium-Ion Battery Anode, *Adv. Mater.*, 2018, **30**(32), 1802074.

27 W. Luo, J. Wan, B. Ozdemir, W. Bao, Y. Chen, J. Dai, H. Lin, Y. Xu, F. Gu, V. Barone and L. Hu, Potassium Ion Batteries with Graphitic Materials, *Nano Lett.*, 2015, **15**(11), 7671–7677.

28 C. Peng, H. Chen, G. Zhong, W. Tang, Y. Xiang, X. Liu, J. Yang, C. Lu and Y. Yang, Capacity fading induced by phase conversion hysteresis within alloying phosphorus anode, *Nano Energy*, 2019, **58**, 560–567.

29 B. Key, R. Bhattacharyya, M. Morcrette, V. Sezne, J.-M. Tarascon and C. P. Grey, Real-Time NMR Investigations of Structural Changes in Silicon Electrodes for Lithium-Ion Batteries, *J. Am. Chem. Soc.*, 2009, **131**, 9239–9249.

30 A. R. Grimmer, ³¹P NMR and π bond in solid phosphorus compounds, *Spectrochim. Acta, Part A*, 1978, **34**(9), 941.

31 S. Hayashi and K. Hayamizu, Spinning-rate dependence of ³¹P magic-angle-spinning nuclear magnetic resonance spectra in condensed phosphates, *Chem. Phys.*, 1991, **157**(3), 381–389.

32 K. Kitada, O. Pecher, P. C. M. M. Magusin, M. F. Groh, R. S. Weatherup and C. P. Grey, Unraveling the Reaction Mechanisms of SiO Anodes for Li-Ion Batteries by Combining *in situ* ⁷Li and ex situ ⁷Li/²⁹Si Solid-State NMR Spectroscopy, *J. Am. Chem. Soc.*, 2019, **141**(17), 7014–7027.

33 W. Li, B. Yan, H. Fan, C. Zhang, H. Xu, X. Cheng, Z. Li, G. Jia, S. An and X. Qiu, FeP/C Composites as an Anode Material for K-Ion Batteries, *ACS Appl. Mater. Interfaces*, 2019, **11**(25), 22364–22370.

34 F. Yang, H. Gao, J. Hao, S. Zhang, P. Li, Y. Liu, J. Chen and Z. Guo, Yolk–Shell Structured FeP@C Nanoboxes as Advanced Anode Materials for Rechargeable Lithium-/Potassium-Ion Batteries, *Adv. Funct. Mater.*, 2019, **29**(16), 1808291.

35 J. Ye, F. Ge, G. Xia, Z. Zheng and C. Hu, CoP nanoflowers with hierarchical nanosheets as high-performance anodes for Li-ion and K-ion batteries, *Mater. Lett.*, 2020, 128687.

36 J. Bai, B. Xi, H. Mao, Y. Lin, X. Ma, J. Feng and S. Xiong, One-Step Construction of N,P-Codoped Porous Carbon Sheets/CoP Hybrids with Enhanced Lithium and Potassium Storage, *Adv. Mater.*, 2018, **30**(35), 1802310.

37 F. Yang, H. Gao, J. Hao, S. Zhang, P. Li, Y. Liu, J. Chen and Z. Guo, Yolk–Shell Structured FeP@C Nanoboxes as Advanced Anode Materials for Rechargeable Lithium-/Potassium-Ion Batteries, *Adv. Funct. Mater.*, 2019, **29**, 1808291.

38 R. Rajagopalan, Y. Tang, X. Ji, C. Jia and H. Wang, Advancements and Challenges in Potassium Ion Batteries: A Comprehensive Review, *Adv. Funct. Mater.*, 2020, **30**(12), 1909486.